Phase Behavior of TDP-43 and hnRNP H1: From Soluble and Aggregated States to Liquid-Like Droplets

Travis R Wang, Jiwu Wang

Allele Biotechnology and Pharmaceuticals, Inc., 6404 Nancy Ridge Drive, San Diego, CA 92121
The Scintillon Institute, 6868 Nancy Ridge Drive, San Diego, CA 92121

Corresponding Author:

Jiwu Wang, Ph.D.
jiwuwang@allelebiotech.com

jiwuwang@scintillon.org

Key Words: TDP-43; hnRNPH1; Phase Separation; Intrinsically Disordered Region; low-complexity domain; SpyTag-SpyCatcher

Abstract (200 words)

Cytotoxic inclusions of TAR DNA-binding protein 43 (TDP-43) have been identified in various neurodegenerative diseases. Mediated by its low-complexity C-terminal domain (CTD), TDP-43 can undergo liquid-liquid phase separation (LLPS) and form aggregates and fibrils. These phase transitions are associated with pathological TDP-43 mislocalization and cytoplasmic aggregation. What determines whether and when TDP-43 adopts a liquid droplet state or forms solid aggregates, transiently or irreversibly? A full understanding of the underlying biophysical mechanisms will help explain the cellular toxicity of aberrant forms of TDP-43 and similar proteins, such as some of the large family of RNA-binding proteins. In this study, we generated recombinant full-length TDP-43 and maintained soluble working solutions without the need of a solubility tag. By focusing on conditions that tune the electrostatic characteristics, we induced phase transitions among states of soluble TDP-43, solid aggregates, and liquid droplet phases in an expedient and controlled manner. We also obtained soluble working solutions of TDP-CTD and another crucial splicing factor, hnRNPH1, and investigated their phase behaviors as individual proteins and their interactions between each other during phase transitions. Using this system, we discovered a previously unreported aggregate-to-droplet transition and found evidence that phase separation of low-complexity domain (LCD)-containing proteins likely involves domain matching when coaggregate out of solution.

Introduction

Protein aggregation is a defining feature of many neurodegenerative disorders, including the accumulation of Tau in Alzheimer's disease, α-synuclein in Parkinson's disease, and TDP-43 in amyotrophic lateral sclerosis (ALS). A central question in ALS study is what stimuli trigger TDP-43 aggregation and which elements and properties of TDP-43 respond to the triggering stimuli. TDP-43 is a ubiquitous RNA-binding protein (RBP) that regulates RNA splicing [1], with roles in regulatory control on mRNA homeostasis, translation, transcription, and transport [2]. Though

42 predominantly residing in the nucleus with an N-terminal nuclear localization signal, TDP-43
43 shuttles between the nucleus and cytoplasm, a process found to be influenced by cellular
44 conditions such as stress [3,4]. The N-terminus region promotes self-association into dimers and
45 ordered oligomers [5], with evidence showing oligomerization into higher-order structures
46 prerequisite to elements of protein function [6,7]. Congruent to its role as an RBP, TDP-43 contains
47 two conserved RNA recognition motifs (RRMs) which mediate binding to RNA and DNA and are
48 central for TDP-43's biological roles. The C-terminus includes a low-complexity domain (LCD)
49 which is glycine-rich and aggregation-prone that regulates protein-protein interactions [8], splicing,
50 and solubility during physiological function [4,7,9].

51

52 Pathologically, the accumulation of TDP-43 aggregates is observed in 90% of cases of ALS, 50%
53 of frontotemporal lobar degeneration cases, and up to 75% in severe cases of Alzheimer's
54 disease, according to some estimates [10]. However, even in physiological functions, TDP-43 does
55 not always exist as a free soluble protein; rather, it transitions between solution and reversible
56 liquid-like droplets (LLDs) with limited mobility [3]. These droplets can change in size and shape in
57 response to cellular conditions. It appears that individual TDP-43 molecules and the oligomer
58 complexes they form exist in a constant state of flux; protein-protein interaction and aggregate
59 formation are always in play without necessarily leading to a pathological endpoint.

60

61 Under stress conditions, TDP-43 relocates to the cytoplasm to scaffold with other RBPs and RNA
62 into dynamic stress granules, which lock down translation and sequester specific molecules as a
63 coordinated cellular response to stress [11,12]. Extensive studies have illustrated that inside stress
64 granules, increased concentration leads to liquid phase separation (demixing) and depletion of
65 native protein [13]. When forming different forms of aggregates, protein concentration and
66 interaction strength among protein molecules are key factors that modulate LLPS from a

67 proteome-wide perspective [14]. One proposed pathway for how soluble TDP-43 congregates and
68 misfolds into toxic aggregates is through prolonged or repeated homotypic-interactions at
69 elevated concentrations within these granules, with other triggers such as oxidative stress, amino
70 acid mutation and modification, and the presence of RNA playing a role [15]. However, studies using
71 tracking and localization microscopy uncovered not only distinct substructures of TDP-43 within
72 stress granules, but also numerous regions of slow-moving TDP-43 species dispersed throughout
73 the cytoplasm, indicating TDP-43 oligomerization and aggregation can also occur inside the
74 cytoplasm but outside of stress granules [16,17], where protein concentrations are not constrained
75 by granule confinement. The precise mechanisms governing the dynamic balance among soluble
76 proteins, oligomer formation, and subsequent transitions into droplets and fibrillar assemblies
77 remain the subject of intense studies but still poorly understood even with significant progress
78 made over a decade by many groups of researchers.

79 The term “aggregate” relevant to LCD-containing RNA-binding proteins commonly refers broadly
80 to oligomers that may be in the form of liquid-like droplets, hydrogel-like “glassy” condensates, or
81 solid formations of various shapes, often progressing in that order [16-18]. Stress granules and
82 similar membraneless organelles, in which most of this process has been studied, dynamically
83 organize protein–protein and protein–RNA interactions in the cytoplasm and through LLPS
84 segregate into a concentrated phase from a dilute phase. LLPS in proteins is often driven by low-
85 complexity domains (LCDs), which mediate multivalent interactions. Both full-length TDP-43 and
86 its C-terminal domain (CTD) are known to undergo phase separation in vitro [14,15].

87 Insoluble inclusions of TDP-43 proteins containing fragments of its C-terminus are a hallmark in
88 numerous neurodegenerative diseases. It is quite remarkable that nearly all pathology-relevant
89 mutations of TDP-43 reside in its CTD [8], indicating the sensitivity of CTD’s intrinsic functions to
90 any sequence perturbation despite its disordered structural morphology. This may suggest that,
91 prior to aggregation, factors beyond structural elements, such as the charges of key amino acids,

92 which can be influenced by extensive phosphorylation, acetylation, and other posttranslational
93 modifications concentrated within the region [8,19]. Additionally, charge distribution along the
94 sequence and neighboring effects, including stacking and hydrophobic interactions with specific
95 charged amino acids, may be essential for their behavior during phase transition [20]. In one report,
96 extensive mutagenesis was conducted to identify amino acid sequence as the "molecular
97 grammar" that dictates phase behavior in the FUS family [21]. In another study, adjusting the
98 placement of charged amino acids within an otherwise hydrophobic sequence resulted in a
99 twofold change in the tendency to phase-separate, without altering the net charge of the
100 polypeptide [22]. To manipulate the phase behaviors of TDP-43 through electrostatic alteration,
101 which shares many similarities with FUS, we created conditions that strongly altered the surface
102 charge of the protein and observed that it drove phase transitions into liquid droplets either directly
103 from soluble protein or, unexpectedly, through a novel reversal pathway from aggregates.
104
105 Phase separation is typically a thermodynamic process that occurs when protein-protein
106 interactions are more favourable than protein-solution interactions, separating proteins and
107 solutes into a dense phase [23]. It has been observed that in cells TDP-43-rich droplets often contain
108 internal vacuoles filled with nucleoplasm materials, and these coexisting yet immiscible
109 multiphase occurrences correlate with ALS-causative mutations in CTD, indicating higher level
110 complexity of phase separation exists and is pathologically relevant [24]. Intriguingly, a reversible
111 double-emulsion structure (droplets-in-droplets) was created in vitro using Poly-rA RNA and PEG
112 and found to be due to kinetic trapping as appose to thermodynamic equilibrium [25], but multi-
113 phase droplets have yet to be recreated with TDP-43 or other similar RNA-binding proteins in vitro
114 in a similarly controlled manner. In this report, we present our system as being able to show multi-
115 emulsion droplet formation with simple triggers and consistent time course.
116

117 The CTD of TDP-43 has been found to form LLDs [26,27]. NMR and in vitro assays identified residue
118 321–335 of TDP-43 in the CTD region to be part of a helical core that tunes LLPS [14] whereas
119 proteolytic and cryo-EM studies identified residue 279-360 as the fibrillar core of TDP-43 filaments
120 [28], encompassing the LLPS core. As for full-length TDP-43, phase separation has been reported
121 under unique poly(ADP-ribose) (PAR) binding conditions with concentrations of TDP-43 at 10μM
122 [29], though in vitro LLPS of the full-length protein is still difficult to induce or control even with
123 favorable conditions such as using crowding agent PEG or aggregation inhibiting molecules
124 dopamine and polyphenol EGCG [30,31]. Here, we present a novel system of manipulating liquid
125 phase separation of CTD and the full-length TDP-43, and for comparison, hnRNPH1. The current
126 paradigm states that TDP-43 LLPS droplets age into hydrogels, inclusions, and amyloid fibrils.
127 LLPS acts as a scaffold accelerating solid aggregate formation, often leading to direct amyloidosis
128 [30]. Our hypothesis is that the phasing-out of the soluble form starts with a "seed" area in a protein-
129 specific manner, which leads to early-stage substructural fibrils, forming solid aggregates or LLDs
130 depending on the charge of this region and subsequent electrostatic interactions. We further show
131 the protein-specific seeding results by using switchable combinations of fluorescent labelling
132 schemes.
133
134 Our findings represent an unusual reversal of the conventional uni-direction liquid-to-solid
135 maturation of protein condensates, showing a more dynamic nature of the 3 macroscopic phases
136 of LCD-containing RNA-binding proteins, and reveal the likely role of electrostatic charge in
137 regulating LLPS.
138
139 **Results and Discussion**
140 **Multidirectional phase transitions of TDP-43 are reversible and tunable**
141 Liquid–liquid phase separation of full-length TDP-43 has been viewed as difficult to create in vitro
142 using recombinant proteins [32]. The few reported cases often relied on an enzymatic cleavage of

143 a solubility tag to initiate aggregation, which is typically monitored by increased turbidity and a
144 process difficult to control [7,33-35]. In other systems, phase separation occurs either almost
145 instantly—within minutes after a solution jump (diluting concentrated protein from storage buffer
146 into phase separation buffer [29]), or very slowly, over 5 days [28]. Both scenarios make it challenging
147 to fine-tune the process or consistently capture time points by design for analysis. To better control
148 the transition process to gain clearer insight into the phase behaviors of these proteins, we sought
149 to generate recombinant full-length TDP-43 of sufficiently high soluble concentration and stability
150 without large solubility tag.
151
152 The first step was to choose a method to keep TDP-43 soluble through purification. Most previous
153 attempts to produce full-length TDP-43 have relied on large solubility tags, such as GST [36], MBP
154 [37], and SUMO [15,28,31], which keep the fusion protein soluble until aggregation is triggered by
155 enzymatic tag cleavage or solution jump. Alternatively, like all proteins, recombinant TDP-43 can
156 be readily solubilized using strong denaturants such as 6-8 M urea or guanidine, with or without
157 a solubilizing tag, and this method has been employed by different investigators [29,36]. However,
158 as complete removal of these denaturants is often problematic because the protein tends to
159 precipitate upon denaturant elimination, a residual low concentration (e.g., ~0.6 M urea or
160 guanidine) is typically retained in storage buffer after purification, which may interfere with subtle
161 aspects of phase behavior. For our in vitro phase analysis system, we aimed to establish a
162 baseline using full-length TDP-43 without interference from large solubility tags or residual
163 denaturants. We chose to produce full-length TDP-43 with only a small His6-tag for purification
164 and use urea to keep it soluble during production, then refold to urea-free storage buffer. We
165 solubilized full-length TDP-43 expressed in E. coli using 6M urea that completely denatured its
166 secondary structures without affecting affinity purification via the His-tag. After washing and
167 eluting with imidazole from cobalt beads in 6 M urea-containing buffers, urea was gradually
168 removed by stepwise dialysis against buffer at 100-fold the sample volume. The urea

169 concentration was reduced by half every 1–2 hours over 5-6 steps, concluding with a final
170 exchange into urea-free buffer.
171
172 As the second step, we formulated the protein storage buffer by first testing whether high or low
173 salt conditions promote solubility. In the field of membraneless organelles and coacervates,
174 critical salt concentration is determined by the intrinsic properties such as charge-to-neutral ratio
175 among monomers of polymeric molecules such as DNA, RNA or protein, and charge distribution
176 and pattern [22,38]. Reducing the salt concentration below the critical salt concentration leads to
177 energy-favorable segregation of many types of proteins. This would suggest that keeping salt
178 concentration high should avoid forming aggregates during purification steps and in storage.
179 Many previous studies indeed used storage buffers containing high salt, e.g. 0.5 M NaCl or KCl
180 [28,31,36,37]. However, we found that TDP-43 tends to aggregate more under high-salt conditions
181 (e.g., 0.5 M NaCl) than under low-salt conditions (Supplementary Fig. 1a). Recent studies have
182 also reported that high salt promotes phase separation of soluble TDP-43 [29,37].
183
184 The fact that high salt destabilizes the soluble state of TDP-43 suggests that charge screening
185 enhances hydrophobic and other non-ionic interactions, thereby promoting phase separation. We
186 hypothesized that similar effects could be achieved by adjusting the buffer pH toward the protein's
187 isoelectric point (pI). To test this, we prepared TDP-43 (5 μM) in a low-capacity pH buffer (20 mM
188 Tris-HCl, pH 8.0) and low salt (100 mM NaCl) and titrated the pH by adding 1 M Tris-HCl at the
189 target pH, maintaining 100 mM NaCl. Approximately 10% of the final volume was required to
190 reach the desired pH. Under these conditions, TDP-43 remained soluble at pH 8.0, but the
191 solution became turbid with diffuse assemblies at pH 7.0. At pH 6.0—near the pI of full-length
192 TDP-43—distinct solid aggregates became evident (Supplementary Fig1b). This observation is
193 consistent with findings from the Chiti group [29], which implied that electrostatic repulsion normally
194 inhibits phase separation. Based on these results, we set the storage buffer for recombinant TDP-

195 43 as 20 mM Tris-HCl, pH 8.0, 100 mM NaCl.

196

197 By combining urea during purification with a solubility-friendly storage buffer, we obtained working
198 solutions of TDP-43 suitable for phase transition analysis. A few points are noteworthy: stepwise
199 removal of urea in our protocol enables the protein to refold through a more controlled process,
200 rather than by dropwise dilution or leaving residual denaturant [29,36]. Complete denaturation with
201 urea also eliminates the need for extensive RNA digestion followed by ion-exchange and gel-
202 filtration chromatography to remove nucleotides, which, if retained, can interfere with phase
203 separation [35].

204

205 To initiate analysis of the solution-to-aggregation transition, we altered salt concentration and pH
206 by adding 5 M NaCl and 1 M Tris-HCl (pH 6.0) to aliquots of TDP-43 (5 μM) storage solution. Once
207 the buffer composition changes to high salt (0.5 M NaCl) at pH 6.0, TDP-43 almost immediately
208 crashed out of solution and forms solid aggregates (Fig 1A). Over several hours, these globules
209 gradually assembled into larger structures composed of subunits that merged into similarly
210 disordered arrangements, reminiscent of fractal-like architectures (Fig. 1a). After 3 hours, these
211 aggregates ranged from clusters of only a few smaller congregates as apparent subunits to
212 assemblies spanning hundreds of microns. The appearance of these structures closely resembles
213 those described by Lashuel and colleagues, which were composed of full-length TDP-43
214 oligomers released from immobilized metal affinity chromatography only in high-imidazole
215 (500 mM) fractions. Unlike our process, their assemblies required approximately five days to form
216 [28]. To assess whether a commonly used solubility tag would alter TDP-43 phase behavior, we
217 tested SUMO, a 101-residue natural fragment with a pI of 5.2. When fused to TDP-43, the
218 resulting construct has a pI of 5.6, close to untagged TDP-43, leading us to predict that both
219 versions would exhibit comparable phase properties under our pH- and salt-based phase
220 transition conditions. We prepared a SUMO–TDP-43 fusion using the same 6 M urea denaturation

221 and renaturation protocol and observed very similar phase behavior (Supplementary Fig. 2a).
222 These results suggest that SUMO tagging preserves TDP-43 phase characteristics and may be
223 suitable for other proteins, although pI matching should be considered.
224
225 Our findings that change in TDP-43 net charge can modulate aggregate formation prompted us
226 to investigate whether alternative strategies for manipulating charge could similarly influence
227 TDP-43 phase behavior. The strong anionic detergent sodium dodecyl sulfate (SDS) micelles
228 facilitate denaturation of protein and destabilization of protein complexes. The extent of
229 destabilization depends on the SDS concentration and the protein−SDS stoichiometry and the
230 resistance to 0.1-2% SDS has been used as a test of TDP-43 fibrillation strength [31,39]. Because
231 SDS introduces negative charges along the entire polypeptide, we therefore employed SDS at a
232 low concentration, 0.03%, as a means of moderating protein surface charge. Upon addition to
233 TDP-43 aggregates, strikingly, the solid aggregates dispersed in the field of view began to 'melt'
234 into glassy material, but instead of dissolving and disappearing, progressively transforming in
235 shape and eventually forming round droplets, in about 6–7 hours (Fig 1b). The droplet formed
236 were quantified in circularity, roundness and solidity in the graph (Fig 1c). Coating aggregated
237 TDP-43 with negative charge via SDS did not dissolve the aggregates into a soluble state but
238 instead transformed them into droplets. We next asked whether introducing net negative charge
239 to soluble TDP-43 would directly induce LLPS. As shown in Fig. 1d, adding SDS to soluble TDP-
240 43 indeed triggered droplet formation, although the droplets were smaller and less dense. These
241 early-phase droplets could be further enlarged and increased in abundance by adding PEG8000
242 (Supplementary Fig. 3), a crowding agent commonly used to promote LLPS [29,36]. The transitions
243 from soluble state to solid aggregates induced by pH and salt, and from soluble state or, as a
244 novel observation, from solid aggregates to liquid-like droplets upon SDS addition are
245 schematically illustrated in Fig 1e.
246

247 The current paradigm for phase separation of LCD-containing RNA-binding proteins describes a
248 progression from soluble molecules to liquid-like condensates, then to glassy solids, and
249 ultimately to amyloid fibers [18]. It is interesting to compare the SDS-induced LLDs with those from
250 adding negative net charge to TDP-43 by other means. For instance, phosphomimetic mutations
251 reduced TDP-43 aggregates and increased the appearance of larger, more liquid-like droplets [33].
252 Inside the cell, phosphorylation is expected to have the similar effects and there are many other
253 factors that can alter the net charge and charge distribution of proteins. McGurk *et al.* reported
254 that non-covalent binding of TDP-43 to poly(ADP-ribose) (PAR), a negatively charged biopolymer
255 and cellular regulator of protein localization and liquid demixing, promotes TDP-43 LLPS in vitro
256 and is essential for its accumulation in stress granules in neurons [15]. Non-covalent binding to PAR
257 resulted in droplets comparable to those in our system using SDS, likely from similar effects of
258 the net charge of TDP-43. As a matter of fact, binding to RNA would add net negative charge to
259 TDP-43 in normal cellular environment, which could enhance LLPS according to our model and
260 indeed suggested by others [40]. Although SDS has not, to our knowledge, been used as a trigger
261 to induce LLPS in TDP-43 or other LCD-containing RNA-binding proteins, it has been reported to
262 promote LLPS of amyloid-β oligomers at supraphysiological concentrations [41], suggesting its
263 broader potential as a tool for modulating phase behavior across diverse proteins. Demonstrating
264 reversibility of solid formations with strong anionic modulators could have significant implications
265 for understanding TDP-43 pathology and developing new therapeutic strategies.
266
267 **SDS-induced droplets possess typical liquid-like properties**
268 Three lines of evidence indicated that droplets derived from solid aggregates shown above exhibit
269 the same liquid properties as those formed by LLPS. First, these droplets fuse upon close contact
270 (Fig. 2a). Second, they dissolve in 1,6-hexanediol, similar to typical LLPS droplets (Fig. 2b).
271 Recent work has shown that glycine and other amino acids can bind phase-separating proteins
272 and modulate condensate stability and liquid-like dynamics [42]. As a third test, we added glycine

273 to the droplets at 50 mM and observed pronounced changes within minutes: dynamic formation
274 of droplets-in-droplets, subsequent growth, and eventual remerging over time (Fig. 2c). These
275 dynamic changes were quantified by tracking the number of internal droplets relative to the size
276 of the encompassing outer droplets (Fig. 2d), as well as the average count over a 12-minute
277 period (Fig. 2e). Upon glycine addition, there was a rapid increase in internal droplet formation,
278 coordinated with the growth of the encompassing droplets. This was followed by a consolidation
279 phase, during which the average number of internal droplets decreased—altogether
280 demonstrating the dynamic liquid-like behavior of these solid-derived droplets.
281
282 When Cy5-labeled mRNA of a fluorescent protein mWasabi as biologically irrelevant mRNA was
283 allowed to bind TDP-43 prior to phase separation, fluorescence imaging revealed that the mRNA
284 colocalized with the protein within the dense phase of the multi-emulsion droplets (Supplementary
285 Fig. 4), consistent with previous findings that full-length TDP-43 oligomers retain RNA-binding
286 capability [31]. These observations indicate that the contents of these droplets exhibit liquid-like
287 properties similar to typical LLPS condensates, despite originating from solid assemblies
288 transformed by forced charge alteration.
289
290 **Phase transition behavior of TDP-43 is generalizable to other RNA-binding proteins.**
291 To see if any of these phase behaviors are specific only to full-length TDP-43, we wanted to
292 compare TDP-43 to hnRNPH1, another nuclear RNA-binding protein that regulates alternative
293 splicing with direct impact on ALS and other diseases [43]. Similar to TDP-43, hnRNPH1 also has
294 a low complexity domain at the C-terminus of the polypeptide composed of 449 residues, close
295 to 414 in TDP-43; its pI is the same at pH 6, allowing us to apply the pH and salt conditions to
296 manipulate the electrostatic and ionic environment for phase transitions established with TDP-43.
297 The CTD of TDP-43 found in neuronal inclusions is composed of ubiquitinated and
298 phosphorylated aggregates of truncated TDP-43 C-terminal (TDP-CTD) fragments of variable

299 sizes between 25 and 35 kDa (e.g., TDP-25 and TDP-35), created by aberrant cleavage events
300 and contribute to ALS [44,45]. TDP-CTD is defined between amino acid 274-414 by early pioneering
301 studies [14,26], or similarly 266-414 [46], 267-414 [27], whereas longer CTD 193-414 has also been
302 studied [47], and all CTD segments have been found to be critical in phase separation as well as
303 aggregations of TDP-43. The 274-414 fragment CTD has a pI close to pH 10. It is previously
304 reported to have a different phase separation response to pH gradients from the full-length [29],
305 likely related to different net charge at different pH compared to the full-length protein. We
306 therefore opted to clone an intermediate-sized version of TDP-CTD, spanning 208 to 414 amino
307 acids, which has a pI at pH 6. This allowed us to compare it to the full-length TDP-43 in parallel
308 and during protein mixing experiments.
309
310 As with full-length TDP-43, both TDP-CTD and hnRNPH1 formed solid assemblies when their
311 solutions were adjusted to pH 6.0 and 0.5 M NaCl. Upon addition of SDS, these assemblies
312 transitioned into droplets, exhibiting behavior broadly similar to that of full-length TDP-43 (Fig. 3a).
313 However, the dynamics and morphological details of the resulting aggregates and droplets varied
314 among the proteins. For example, TDP-CTD consistently formed larger and more compact
315 aggregates compared to TDP-43 and hnRNPH1. Whilst the primary focus of this report is to
316 demonstrate macroscale phase transition processes that can be modulated by solution
317 conditions, further insights could be gained by examining the fine structural differences underlying
318 the various assembly forms of these proteins. This result nevertheless supports that the pI and
319 high salt promotion of solid aggregation and their SDS-induced conversion into droplets are not
320 specific to full-length TDP-43, which is expected according to the notion that a generalizable
321 mechanism based on electrostatic and hydrophobic interactions could dictate phase behavior.
322
323 TDP-CTD droplets and aggregates are known to contain amyloid filaments [27,48,49]. To examine
324 the amyloid nature of our TDP-43 and TDP-CTD solid aggregates, we stained them with classical

325 amyloid-binding dyes, including thioflavin-T (ThT) and Congo Red (CR), both of which strongly
326 fluoresce upon binding to β-sheet-rich amyloid structures. They exhibited clear and nearly uniform
327 positive staining, suggesting that amyloid structures are present throughout the formations and
328 likely organized at the substructural level rather than being confined to larger, assembled
329 structures (Fig 3b). Next, we stained the droplets formed from both TDP-43 and TDP-CTD solid
330 aggregates with SDS addition and discovered that these droplets too were remarkably ThT and
331 CR positive (Fig 3c). Extensive studies by many groups on LLPS of TDP-CTD have shown that
332 amyloid fibrillation can occur independently of LLPS, as observed in our solid aggregates;
333 whereas ThT-positive amyloid fibrils have also been detected within liquid droplets, consistent
334 with our findings in solid-derived droplets [27,50]. Future investigations using high-resolution imaging
335 should reveal how proteins within these enclosures organize into oligomers assembling into
336 amyloids or amyloid precursors, potentially originating from the helical structures present in both
337 full-length TDP-43 and its CTD during assembly transitions, giving rise to β-sheet-rich structures
338 [26,39,46].
339
340 The formation of multi-emulsion or mulitphase droplets is a characteristic feature of complex
341 coacervate (polyelectrolyte material) mixtures, widely viewed as models for studying charge-
342 mediated LLPS [38]. By patterning charged monomers along a polymer backbone such as
343 polypeptides, one can precisely adjust local charge organization and the resulting electrostatic
344 interactions between coacervate-forming chains, creating multi-phase or multi-emulsion droplets
345 [22]. In TDP-43, charged amino acids are naturally distributed along the polypeptide, with additional
346 charges that can be introduced in vivo through phosphorylation and other post-translational
347 modifications, particularly concentrated in the CTD. In our in vitro phase-separation system, a
348 droplets-in-droplets morphology can be induced simply by adding glycine to SDS-induced
349 droplets (Fig 2c). As previously reported, glycine interacts weakly with amide groups in the protein
350 backbone and aromatic side chains, reducing backbone–backbone contacts while enhancing

351 interactions among aromatic residues [42]. The biological relevance lies in the surprising
352 observation that free amino acids account for more than 25% of the total volume and 6% of the
353 total dry mass of a mammalian cell [51], as well as their natural role in stabilizing proteins and
354 colloidal dispersions [52]. We set out to determine the nature of multi-emulsion droplets formed
355 following glycine addition to SDS-induced single droplets. To do this, we repeated the experiment
356 shown in Figure 2c but in the presence of ThT, and used confocal imaging to visualize phase
357 behavior and amyloid properties. Z-stacks of representative complex droplets revealed alternating
358 dense (coacervate) and dilute (supernatant) phases within larger droplets (Fig. 3d). The 'bubbles'
359 were ThT-negative, whereas the coacervates were ThT-positive, confirming the presence of
360 amyloid substances in protein-rich coacervates at the 3D level. This result further highlights the
361 liquid-like dynamics of SDS-induced droplets and the secondary phase separation that can be
362 triggered by electrostatic effectors such as glycine.
363
364 **Amyloid formation starts upon phase separation**
365 Unlike the CTD of TDP-43, findings on the phase separation behavior of full-length TDP-43 and
366 the role of amyloid fibrillation are less consistent, partly due to the challenges of producing
367 recombinant full-length TDP-43 without large solubility tags or denaturing agents such as urea,
368 even at low concentrations [32]. Among the few studies on full-length TDP-43, some reported
369 aggregates composed of proteins with disordered secondary structure that failed to bind ThT
370 [19,53,54]. Other studies observed ThT-positive segregated structures, but the process required
371 extended time, approximately 10 hours in one case [55] and 9 days with agitation in another [56].
372 Understanding this time course may provide valuable insights into the fibrillation pathway,
373 including the involvement of LLPS or solid aggregates, and is essential for clarifying how disease-
374 associated amyloid fibrils form. Leveraging the controllability of aggregate and droplet formation
375 using our solubility tag-free recombinant proteins and their strong ThT staining once high order
376 structures form, we performed fluorescence video recording to capture the dynamic process of

377 TDP-43 solutions transitioning into droplets with SDS or forming solid aggregates under
378 conditions of pH near the isoelectric point and high salt. Time-lapse images extracted from videos
379 recorded at fixed fields of view from two independent repeats show that, upon addition of SDS to
380 0.03% at time zero, small droplets began to emerge and progressively increased in size, through
381 joining from soluble proteins or by merging (Fig. 4a). Notably, ThT, present in the protein solution
382 prior to SDS addition, stained both small and large droplets within the first captured time point.
383 While fluorescence intensity increased over time, the rate of increase appeared generally in line
384 with the growth in droplet size, with a slight delay that could reflect amyloid fibrillation progressed
385 in addition to droplet growth; the total droplet counts increased during the first 4 hours before
386 decreasing through merging (Fig. 4b, Supplementary Videos). A low concentration of glycine at
387 5mM, 10% of what was used in Fig 2c, was also included, and by hour 7, double-emulsion droplets
388 shown as dark circles began to appear, consistent with the results shown in Fig. 2c but at a slower
389 pace. We then applied the same video recording approach to monitor solid aggregate formation
390 from soluble solutions. Similar to SDS-induced droplet formation, aggregates triggered by pH near
391 the isoelectric point and high salt were stained by ThT shortly after induction. These amorphous,
392 fractal-like solids continued to grow, originating entirely from recruiting soluble protein, as no
393 merging events were observed (Fig 4c). Analysis of the area and intensity of the solid formations
394 supports our interpretation that aggregates rapidly grew from unstained protein molecules and
395 began to plateau at around 3 hours (Fig. 4d). These observations were consistent across multiple
396 trials and variations using different imaging systems, all showing a smooth transition from
397 unstained solution to clear and immediate amyloid-positive staining. This behavior contrasts with
398 some of the previous reports on full-length TDP-43, as discussed above. The discrepancy may
399 stem from our approach: the protein was fully denatured and then slowly renatured, likely
400 maintaining a more native-like conformation. Additionally, induction was carried out by adding the
401 triggering solution at less than 10% of the final volume, creating lower perturbation or stress to
402 the system than other protocols, perhaps better reflecting biological events in vivo.

403

404 **Switchable fluorescent protein tags are a valuable tool for studying protein phase behavior**

405 We were also interested in determining whether different proteins, sharing the same or similar but
406 distinct LCDs, would co-aggregate or remain segregated upon triggering phase separation. To
407 address this, we designed a system to track multiple proteins using distinguishable fluorescent
408 labels. Because phase separation in our system depends on charges that influence electrostatic
409 and hydrophobic interactions, we avoided commonly used dyes that bind to amino acids and may
410 alter charge. Structural dyes such as ThT and CR are unsuitable for aggregate combination
411 studies because they lack protein-specific tracking capability. Instead, we adapted a switchable
412 tagging system to label TDP-43, TDP-CTD, and hnRNPH1 with spectrally distinct fluorescent
413 proteins. A 13-amino-acid SpyTag was added to the C-terminus of each protein via a 7-amino-
414 acid linker, and the 116-amino-acid SpyCatcher was fused to the N-terminus of mNeonGreen [57],
415 mScarlet3 [58], and mTurquoise2 [59], fluorescent proteins (FP) with optimal brightness, physical and
416 photo stability, and more stringent monomeric properties within their respective spectrum to
417 maximize fluorescence signal while minimizing aggregation artifacts (Fig. 5a). By briefly mixing a
418 pair of SpyTag- and SpyCatcher-fused proteins, a fluorescent label is covalently attached to the
419 target protein via SpyTag–SpyCatcher bonding. The protein ratios within each pair were
420 optimized, with a slight excess of SpyCatcher-FP to ensure that all SpyTags on target proteins
421 were occupied (SFig 5).

422

423 The pI of all three SpyCatcher-FPs ranges between 5.0 and 5.5. When fused with TDP-43, TDP-
424 CTD, or hnRNPH1, the resulting fusion proteins have a pI between 5.5 and 6.0, predicting low
425 net charge like the untagged proteins under our aggregation induction conditions. As expected,
426 when the buffer was adjusted to pH 6.0 with 0.5M NaCl, the fused proteins formed solid
427 aggregates, exhibiting strong and uniform fluorescence (Fig. 5b). Each protein can be fused to
428 any FP without apparent differences in behavior when the FP was switched among the three

429 monomeric variants (Supplementary Fig 6). We concluded that adding an FP to the C-terminus
430 of these proteins does not significantly alter their phase behavior; rather, it affords a convenient
431 and switchable end labeling system for studying these proteins that may benefit the field. Older
432 versions of green and red FPs have been used in fusions to study TDP-43 both in vivo and in
433 vitro [37,53,60]. Our data align with these findings, indicating that FP tags offer reliable information
434 about native proteins. Most commonly used FPs have a slightly acidic pI, making them unlikely to
435 interfere with pH-dependent effects on net charge or electrostatic interactions of proteins with
436 similar pI like TDP-43. However, caution may be warranted about the tendency of conventional
437 avGFP-derived GFP and YFP and their variations to form weak dimers [61] in studies of
438 oligomerization and seeding for aggregation.
439
440 With fluorescence signals appended to each protein, we performed time-lapse imaging to track
441 the transition of individual aggregates of TDP-43 and TDP-CTD fused to mScarlet3 and
442 mNeonGreen, respectively. Spread-out aggregates of either protein began condensing within 10
443 minutes of SDS addition and self-merged into spheroid structures within 1 hour (Fig. 5C), in
444 agreement with results shown using non-fusion TDP-43 (Fig 1b).
445
446 **Electrostatic-driven phase separation is differential to aggregation seeding**
447 Having observed that TDP-43, its CTD, and hnRNPH1, a distinct protein with comparable features
448 to TDP-43—all exhibited parallel behaviors, and equipped with FP tagging to spectrally tracking
449 them through phase transition processes, we explored whether phase separation is directed by
450 protein-specific features, or if it is a more generic physical property-driven process such as
451 hydrophobic inclusion. We pairwise-mixed all three proteins, each tagged with a different FP, and
452 examined aggregates for the presence of two different proteins. Interestingly, coaggregates were
453 readily observed between full-length TDP-43 and TDP-CTD (Fig. 6). However, in all view areas

454 obtained from repeated attempts, no coaggregates were detected between hnRNPH1 and either
455 TDP-43 or TDP-CTD. Because TDP-CTD is a segment of TDP-43 and known to be required for
456 phase separation [24,26], we hypothesized that the cocomplex between TDP-43 and TDP-CTD
457 forms through the shared helical seed within the LLPS core previously identified by biochemical
458 and structural studies [14,28]. On the other hand, although hnRNPH1 contains its own LCD at the
459 C-terminus, also involved in phase separation [43], its core sequence differs from that of TDP-43.
460 These results suggest that protein assembly is not driven solely by hydrophobic or other
461 nonspecific physical forces, as the process is not protein-agnostic. Instead, it is plausible that
462 under conditions controlling electrostatic interactions combined with hydrophobic segregation
463 from the aqueous phase, proteins initiate phase separation at their LCD cores. These regions,
464 with accessibility and flexibility, may allow transient 'kiss-and-run' interactions when no matching
465 partner is found, or bundle to form fibrils and develop amyloids when matching occurs. Recent
466 efforts started to illustrate noncanonical mechanism of protein recognition wherein transient
467 interactions surrounding the TDP-43 conserved helical region drive the phase separation of CTD
468 through direct enhancement of site-specific, helix-mediated interactions, providing an example of
469 how sequence can be used as a code for segregation [62]. It was previously reported that the
470 mutations within the core of 279-360 (as defined by Kumar *et al.* [28]) rendered TDP-43 less liquid-
471 like [24], and led to defect in stress granule formation [63]. The sequence specificity in multiple protein
472 assembly formation revealed by our results could have implications in understanding the effects
473 of these mutations.
474
475 **Towards modulation of phase transition**
476 Based on the experimental data presented in this study, we propose a unifying perspective about
477 phase behavior of proteins such as TDP-43: electrostatics related to charge, whether global or
478 localized, arising from natural amino acid composition and post-translational modifications, or, in
479 vitro, attunement to pH, salt screen, zwitterionic glycine (and other amino acids) or charge

480 decoration by ionic detergent SDS, can dictate how proteins like TDP-43 transition among various
481 macroscopic phases while possibly maintaining some microscopic substructures while shifting
482 others (e.g. dimers, oligomers, nonamyloid fibrils and amyloids) to reach the lowest-energy steady
483 state. These states all retain a degree of fluidity and reversibility, allowing the system to respond
484 dynamically to environmental changes.
485
486 Protein assemblies can be visualized at the micron scale using optical microscopy, as shown in
487 this study, or at the nanometer scale with electron microscopy and other high-resolution
488 techniques, revealing details such as filaments containing a β-sheet-rich helical amyloid core [28].
489 Large assemblies likely originate from smaller subunits that act as building blocks, beginning as
490 oligomers and progressing through stepwise assembly, a process typically slow, occurring over
491 hours or days [31], though notably faster in our system. These substructures may share physical
492 and chemical characteristics with the larger assemblies they form, either through fractal growth
493 into amorphous solids or by coexisting in a milieu that phase-separates into liquid-like droplets.
494 In our system, strong ThT and CR staining were observed in both solids and droplets, during or
495 after solid-to-droplet transitions with no transition delays, suggesting different formations might
496 share related substructures. They may originate from a seed region containing an amphipathic
497 helix shared among aggregating molecules [29], undergoing conformational transitions toward
498 increased β-sheet stacking during maturation, under stress, or with mutations, as previously
499 proposed [30,49,64]. Such seeding could allow the initial helical core and adjacent sequences to act
500 as a sorting mechanism, determining interaction partners and conditions. It is important to note
501 that RNA-binding proteins can also interact one-to-one as soluble molecules via LCDs, such as
502 glycine-rich regions, to perform biological functions like alternative splicing without undergoing
503 phase transitions, as shown in our earlier in vitro protein-protein interaction studies [65,66].
504
505 TDP-43 is known to co-segregate under physiological conditions with numerous other proteins,

506 including hnRNPA1, hnRNPA2, and FUS [3,67,68], through domain-specific physical contact, via
507 RNA binding, or perhaps also coaggregation based on matching helix or β-sheet stacking at seed
508 region, which will be interesting to test. The phase transitions observed here with TDP-43 and
509 hnRNPH1 may extend beyond RNA-binding proteins involved in splicing regulation. A notable
510 early example is Sear's 2007 prediction that the Dvl protein would undergo LLPS [69], an all-or-
511 none switch that has since been shown to play a critical role in the Wnt signaling pathway [70].
512
513 The discovery that solid aggregates can be driven into a more liquid-like state may open new
514 avenues for identifying therapeutic intervention points by preserving normal, reversible LLPS that
515 does not progress to irreversible fibril amyloid formation [71]. Potential strategies include using short
516 RNAs to provide specificity by targeting RNA-binding proteins, and amino acids or oligopeptides
517 to achieve charge-modifying effects.
518
519 **Materials and Methods**
520 **Protein production**
521 Plasmids encoding TDP-43, TDP-CTD, hnRNPH1, and SUMO–TDP-43 were cloned into the
522 pNCS vector [57] and transformed into NEB SHuffle E. coli competent cells. Selected colonies were
523 inoculated into culture tubes containing 5mL 0.1 mg/mL carbenicillin 2xYT broth and incubated at
524 30°C overnight while shaking, the next day transferred to 500mL 2xYT broth and again incubated
525 overnight while shaking. For expression, small culture transformed bacteria were cultured in 500
526 mL 2×YT broth supplemented with 0.1 mg/mL carbenicillin at 30°C while shaking overnight. Cells
527 were harvested by centrifugation at 8,000 × g, and the pellets were resuspended in lysis buffer
528 containing 20 mM Tris-HCl (pH 8.0), 6 M urea, 500 mM NaCl, and 10 mM imidazole.
529
530 Cells were lysed by sonication on ice (30% amplitude, 5 min total, 10 s on/10 s off) and centrifuged
531 at 8,000 × g to remove debris. The supernatant was incubated at 4 °C for 1 h to overnight with

532 nickel beads to capture His-tagged proteins. Bead–protein complexes were transferred to
533 purification columns and washed 3–4 times with wash buffer (20 mM Tris-HCl, pH 8.0; 500 mM
534 NaCl; 10 mM imidazole; 6 M urea). Proteins were eluted in a single step using elution buffer (20
535 mM Tris-HCl, pH 8.0; 500 mM NaCl; 200 mM imidazole; 4.5 M urea) and filtered through 0.22 μm
536 PES syringe filters.
537
538 Protein purity was assessed by SDS-PAGE, and concentrations were measured using NanoDrop.
539 Eluted proteins were standardized to 5 μM, or about 0.2mg/ml, after removal of urea in gradual
540 5-6 step dialysis using Spectra/Por dialysis tubing (MW cutoff 7,000) against storage buffer of 20
541 mM Tris-HCl, pH 8.0 100 mM NaCl with urea concentration decreasing ~50% per step until all
542 urea was removed. Soluble protein was collected and stored at −20 °C.
543
544 **Formation of solid aggregates**
545 Phase separation reactions for TDP-43, TDP-CTD, and hnRNPH1 were initiated from soluble
546 protein fractions by adjusting the storage buffer from pH 8 to pH 6 using small-volume additions
547 of 1 M pH buffer. Additional modifications, such as changes in salt concentration, were made by
548 adding small volumes of high-molarity salt solutions. The total reaction volume was approximately
549 40 μL. All added reagents to modify experimental conditions resulted <10% increase to the total
550 reaction volume. Aggregates from all proteins were monitored at designated time points, with
551 complete formation typically occurring within 5 hours.
552
553 **Formation of liquid-like condensates**
554 Liquid-like condensates were generated from either soluble proteins or pre-formed solid
555 aggregates by adding SDS directly to the reaction mixture. The transition typically completed
556 within 8 hours. The final SDS concentration was 0.03%, consistent across all stated methods.
557

558 In experiments where glycine was added to probe the effects of addition, the final concentration
559 of glycine was 50 mM for experiments shown in Fig 2c, and 5mM in Fig 4a. Concentrated glycine
560 was diluted directly to the experimental conditions.
561
562 To quantify droplet shape characteristics, three geometric descriptors were calculated from binary
563 images: circularity, roundness, and solidity.
564 Circularity was calculated using the formula:
565 $\text{Circularity} = (4 \times \pi \times \text{Area}) / (\text{Perimeter}^2)$
566 This metric ranges from 0 to 1, where a value of 1 indicates a perfect circle. Lower values suggest
567 more elongated or irregular shapes.
568
569 Roundness was defined as:
570 $\text{Roundness} = (4 \times \text{Area}) / (\pi \times (\text{Major Axis Length})^2)$
571 Roundness also ranges from 0 to 1, with higher values indicating shapes closer to a perfect circle,
572 but it is more sensitive to elongation than circularity.
573
574 Solidity was computed as:
575 $\text{Solidity} = \text{Area} / \text{Convex Hull Area}$
576 Solidity measures the extent to which a shape is convex. A value of 1 indicates a completely
577 convex shape, while lower values suggest the presence of concavities or irregular boundaries.
578 All measurements were performed using image analysis software capable of extracting shape
579 descriptors from segmented droplet images.
580
581 **Imaging**
582 Microscopy imaging included bright-field, phase contrast, widefield fluorescence, and confocal
583 fluorescence modalities. The primary instrument was the Keyence BZ-X800 fluorescence

584 microscope for both light and fluorescence imaging. Additional bright-field and widefield
585 fluorescence images were captured using the EVOS FL Fluorescence Digital Microscope, while
586 confocal fluorescence imaging was performed with the BioTek Cytation C10 Confocal Imaging
587 Reader. Images taken by Cytation C10 were at 40x magnification. All other images were taken at
588 20x magnification.
589
590 **Image analysis and quantifications**
591 Image contrast and brightness were adjusted uniformly for clarity using ImageJ. Quantitative
592 measurements were also performed using ImageJ's built-in analysis functions.
593
594 For quantifications of fluorescence images, ImageJ's color threshold function was used to
595 delineate positive signals from background signal. The analysis function provided a count of
596 detected structure, the area covered by structures of the total visible area Area%, as well as
597 fluorescence intensity IntDen.
598
599 IntDen or Integrated Density is the product of mean gray value (a stand-in for intensity) and area,
600 representing the amount of dye bound and fluorescing. The units are (relative fluorescence units)
601 * (μm^2). Corrected Total View Fluorescence is used to represent the intensity of fluorescence in
602 our measurements, which takes the IntDen value from each measured object and corrects for
603 background fluorescence. The equation is as follows:
604 IntDen – (Area of Droplet * Mean fluorescence of background)
605 The mean fluorescence of background was measured by averaging 3 separate readings of the
606 background for each time point and view of the well.
607
608 **Dye staining**
609 Protein assemblies were stained by incubating at room temperature for 2–3 hours with Thioflavin

610 T (ThT) or Congo Red (CR) from Sigma. Final concentrations in wells were 40 μM ThT or 0.5%
611 CR. For time course experiments shown in Fig 4, ThT was added to the solution before the phase
612 separation was triggered.
613
614 **SpyTag/SpyCatcher Conjugation**
615 Protein constructs were conjugated by incubating together at room temperature for 1 hour. FP–
616 SpyCatcher was added in slight excess (10%) over IDP–SpyTag to achieve a 1.1:1 molar ratio.
617 For quenching, excess SpyTag-tagged nanobodies (at least 4× the molarity of SpyCatcher–FP)
618 were added to bind any remaining free SpyCatcher–FP, followed by an additional 1-hour
619 incubation at room temperature.
620
621 **Acknowledgment**
622 We thank Alex Ward for DNA constructions and initial attempts at protein production, Andrew
623 Chammas and Nathan Shaner for help with acquisition of SpyTag and SpyCatcher constructs,
624 Aryan Mudliar for lab assistance and discussions.
625
626 **Author Contributions**
627 JW conceptually initiated the project; TRW designed and carried out the experiments; TRW and
628 JW interpreted data and drafted the manuscript.
629
630 **Competing Interest**
631 JW is a current employee of Allele Biotech, a biotech company in the US.
632
633 **Data Availability**

634 Additional, related data of the present report is available from the corresponding author upon
635 reasonable request.
636

637 **Supplementary Material**

638 Supplementary material.doc: Supplementary figures, materials and methods

639 Movie S1: Continued droplet development example 2

640 Movie S2: Continued droplet development example 2

641

642 **References**

643 1 Polymenidou, M. *et al.* Long pre-mRNA depletion and RNA missplicing contribute to
644 neuronal vulnerability from loss of TDP-43. *Nat Neurosci* **14**, 459-468 (2011).
645 https://doi.org/10.1038/nn.2779
646 2 Ishiguro, T. *et al.* Regulatory Role of RNA Chaperone TDP-43 for RNA Misfolding and
647 Repeat-Associated Translation in SCA31. *Neuron* **94**, 108-124 e107 (2017).
648 https://doi.org/10.1016/j.neuron.2017.02.046
649 3 Gasset-Rosa, F. *et al.* Cytoplasmic TDP-43 De-mixing Independent of Stress Granules
650 Drives Inhibition of Nuclear Import, Loss of Nuclear TDP-43, and Cell Death. *Neuron* **102**,
651 339-357 e337 (2019). https://doi.org/10.1016/j.neuron.2019.02.038
652 4 Ayala, Y. M. *et al.* Structural determinants of the cellular localization and shuttling of TDP-
653 43. *J Cell Sci* **121**, 3778-3785 (2008). https://doi.org/10.1242/jcs.038950
654 5 Shiina, Y., Arima, K., Tabunoki, H. & Satoh, J. TDP-43 dimerizes in human cells in culture.
655 *Cell Mol Neurobiol* **30**, 641-652 (2010). https://doi.org/10.1007/s10571-009-9489-9
656 6 Perez-Berlanga, M. *et al.* Loss of TDP-43 oligomerization or RNA binding elicits distinct
657 aggregation patterns. *EMBO J* **42**, e111719 (2023).
658 https://doi.org/10.15252/embj.2022111719
659 7 Wang, A. *et al.* A single N-terminal phosphomimic disrupts TDP-43 polymerization, phase
660 separation, and RNA splicing. *EMBO J* **37** (2018).
661 https://doi.org/10.15252/embj.201797452
662 8 Santamaria, N., Alhothali, M., Alfonso, M. H., Breydo, L. & Uversky, V. N. Intrinsic disorder
663 in proteins involved in amyotrophic lateral sclerosis. *Cell Mol Life Sci* **74**, 1297-1318
664 (2017). https://doi.org/10.1007/s00018-016-2416-6
665 9 Buratti, E. *et al.* TDP-43 binds heterogeneous nuclear ribonucleoprotein A/B through its
666 C-terminal tail: an important region for the inhibition of cystic fibrosis transmembrane
667 conductance regulator exon 9 splicing. *J Biol Chem* **280**, 37572-37584 (2005).
668 https://doi.org/10.1074/jbc.M505557200

669 10 Jo, M. *et al.* The role of TDP-43 propagation in neurodegenerative diseases: integrating
670 insights from clinical and experimental studies. *Exp Mol Med* **52**, 1652-1662 (2020).
671 https://doi.org/10.1038/s12276-020-00513-7
672 11 Lang, R., Hodgson, R. E. & Shelkovnikova, T. A. TDP-43 in nuclear condensates: where,
673 how, and why. *Biochem Soc Trans* **52**, 1809-1825 (2024).
674 https://doi.org/10.1042/BST20231447
675 12 Lee, Y. B. *et al.* Cytoplasmic TDP-43 is involved in cell fate during stress recovery. *Hum Mol*
676 *Genet* **31**, 166-175 (2021). https://doi.org/10.1093/hmg/ddab227
677 13 Chen, Y. & Cohen, T. J. Aggregation of the nucleic acid-binding protein TDP-43 occurs via
678 distinct routes that are coordinated with stress granule formation. *J Biol Chem* **294**, 3696-
679 3706 (2019). https://doi.org/10.1074/jbc.RA118.006351
680 14 Conicella, A. E. *et al.* TDP-43 alpha-helical structure tunes liquid-liquid phase separation
681 and function. *Proc Natl Acad Sci U S A* **117**, 5883-5894 (2020).
682 https://doi.org/10.1073/pnas.1912055117
683 15 McGurk, L. *et al.* Poly(ADP-Ribose) Prevents Pathological Phase Separation of TDP-43 by
684 Promoting Liquid Demixing and Stress Granule Localization. *Mol Cell* **71**, 703-717 e709
685 (2018). https://doi.org/10.1016/j.molcel.2018.07.002
686 16 Fonda, B. D., Jami, K. M., Boulos, N. R. & Murray, D. T. Identification of the Rigid Core for
687 Aged Liquid Droplets of an RNA-Binding Protein Low Complexity Domain. *Journal of the*
688 *American Chemical Society* **143**, 6657-6668 (2021). https://doi.org/10.1021/jacs.1c02424
689 17 Lin, Y., Protter, D. S., Rosen, M. K. & Parker, R. Formation and Maturation of Phase-
690 Separated Liquid Droplets by RNA-Binding Proteins. *Mol Cell* **60**, 208-219 (2015).
691 https://doi.org/10.1016/j.molcel.2015.08.018
692 18 Shin, Y. & Brangwynne, C. P. Liquid phase condensation in cell physiology and disease.
693 *Science* **357** (2017). https://doi.org/10.1126/science.aaf4382
694 19 Johnson, B. S. *et al.* TDP-43 is intrinsically aggregation-prone, and amyotrophic lateral
695 sclerosis-linked mutations accelerate aggregation and increase toxicity. *J Biol Chem* **284**,
696 20329-20339 (2009). https://doi.org/10.1074/jbc.M109.010264
697 20 François-Moutal, L. *et al.* Structural Insights Into TDP-43 and Effects of Post-translational
698 Modifications. *Frontiers in Molecular Neuroscience* **12** (2019).
699 https://doi.org/10.3389/fnmol.2019.00301
700 21 Wang, J. *et al.* A Molecular Grammar Governing the Driving Forces for Phase Separation
701 of Prion-like RNA Binding Proteins. *Cell* **174**, 688-699 e616 (2018).
702 https://doi.org/10.1016/j.cell.2018.06.006
703 22 Chang, L. W. *et al.* Sequence and entropy-based control of complex coacervates. *Nat*
704 *Commun* **8**, 1273 (2017). https://doi.org/10.1038/s41467-017-01249-1
705 23 Millar, S. R. *et al.* A New Phase of Networking: The Molecular Composition and Regulatory
706 Dynamics of Mammalian Stress Granules. *Chem Rev* **123**, 9036-9064 (2023).
707 https://doi.org/10.1021/acs.chemrev.2c00608
708 24 Schmidt, H. B. & Rohatgi, R. In Vivo Formation of Vacuolated Multi-phase Compartments
709 Lacking Membranes. *Cell Rep* **16**, 1228-1236 (2016).
710 https://doi.org/10.1016/j.celrep.2016.06.088

711 25 Erkamp, N. A. *et al.* Spatially non-uniform condensates emerge from dynamically arrested
712 phase separation. *Nature Communications* **14** (2023). https://doi.org/10.1038/s41467-
713 023-36059-1
714 26 Conicella, A. E., Zerze, G. H., Mittal, J. & Fawzi, N. L. ALS Mutations Disrupt Phase
715 Separation Mediated by alpha-Helical Structure in the TDP-43 Low-Complexity C-Terminal
716 Domain. *Structure* **24**, 1537-1549 (2016). https://doi.org/10.1016/j.str.2016.07.007
717 27 Babinchak, W. M. *et al.* The role of liquid-liquid phase separation in aggregation of the
718 TDP-43 low-complexity domain. *J Biol Chem* **294**, 6306-6317 (2019).
719 https://doi.org/10.1074/jbc.RA118.007222
720 28 Kumar, S. T. *et al.* Seeding the aggregation of TDP-43 requires post-fibrillization
721 proteolytic cleavage. *Nature Neuroscience* **26**, 983-996 (2023).
722 https://doi.org/10.1038/s41593-023-01341-4
723 29 Staderini, T., Bigi, A., Mongiello, D., Cecchi, C. & Chiti, F. Biophysical characterization of
724 full-length TAR DNA-binding protein (TDP-43) phase separation—solution-jump. *Protein*
725 *Sci* **31**, e4509 (2022). https://doi.org/10.1002/pro.4509
726 30 Liu, Y. *et al.* The Regulation of TDP-43 Structure and Phase Transitions: A Review. *Protein*
727 *J* **44**, 113-132 (2025). https://doi.org/10.1007/s10930-025-10261-0
728 31 Yang, L., Jasiqi, Y. & Lashuel, H. Recombinant Full-Length TDP-43 Oligomers Retain Their
729 Ability to Bind RNAs, Are Not Toxic, and Do Not Seed TDP-43 Aggregation in Vitro. *ACS*
730 *Chem Neurosci* **15**, 193-204 (2024). https://doi.org/10.1021/acschemneuro.3c00691
731 32 Staderini, T. *et al.* Biophysical characterization of the phase separation of TDP-43 devoid
732 of the C-terminal domain. *Cell Mol Biol Lett* **29**, 104 (2024).
733 https://doi.org/10.1186/s11658-024-00615-4
734 33 Gruijs Da Silva, L. A. *et al.* Disease‐linked TDP‐43 hyperphosphorylation suppresses
735 TDP‐43 condensation and aggregation. *The EMBO Journal* **41** (2022).
736 https://doi.org/10.15252/embj.2021108443
737 34 Mann, J. R. *et al.* RNA Binding Antagonizes Neurotoxic Phase Transitions of TDP-43.
738 *Neuron* **102**, 321-338 e328 (2019). https://doi.org/10.1016/j.neuron.2019.01.048
739 35 Molliex, A. *et al.* Phase separation by low complexity domains promotes stress granule
740 assembly and drives pathological fibrillization. *Cell* **163**, 123-133 (2015).
741 https://doi.org/10.1016/j.cell.2015.09.015
742 36 Vivoli Vega, M. *et al.* Isolation and characterization of soluble human full-length TDP-43
743 associated with neurodegeneration. *FASEB J* **33**, 10780-10793 (2019).
744 https://doi.org/10.1096/fj.201900474R
745 37 Krainer, G. *et al.* Reentrant liquid condensate phase of proteins is stabilized by
746 hydrophobic and non-ionic interactions. *Nature Communications* **12** (2021).
747 https://doi.org/10.1038/s41467-021-21181-9
748 38 Lu, T. & Spruijt, E. Multiphase Complex Coacervate Droplets. *J Am Chem Soc* **142**, 2905-
749 2914 (2020). https://doi.org/10.1021/jacs.9b11468
750 39 Garg, D. K. & Bhat, R. Modulation of assembly of TDP-43 low-complexity domain by
751 heparin: From droplets to amyloid fibrils. *Biophysical Journal* **121**, 2568-2582 (2022).
752 https://doi.org/10.1016/j.bpj.2022.05.042

753 40 Wang, C. *et al.* Stress Induces Dynamic, Cytotoxicity-Antagonizing TDP-43 Nuclear Bodies
754 via Paraspeckle LncRNA NEAT1-Mediated Liquid-Liquid Phase Separation. *Mol Cell* **79**,
755 443-458 e447 (2020). https://doi.org/10.1016/j.molcel.2020.06.019
756 41 Gui, X. *et al.* Liquid-liquid phase separation of amyloid-beta oligomers modulates amyloid
757 fibrils formation. *J Biol Chem* **299**, 102926 (2023).
758 https://doi.org/10.1016/j.jbc.2023.102926
759 42 Xu, X. *et al.* Amino acids bind to phase-separating proteins and modulate biomolecular
760 condensate stability and dynamics. *Nature Communications* **16** (2025).
761 https://doi.org/10.1038/s41467-025-63755-x
762 43 Kim, G. H. & Kwon, I. Distinct roles of hnRNPH1 low-complexity domains in splicing and
763 transcription. *Proc Natl Acad Sci U S A* **118** (2021).
764 https://doi.org/10.1073/pnas.2109668118
765 44 Neumann, M. *et al.* Ubiquitinated TDP-43 in frontotemporal lobar degeneration and
766 amyotrophic lateral sclerosis. *Science* **314**, 130-133 (2006).
767 https://doi.org/10.1126/science.1134108
768 45 Zhang, Y. J. *et al.* Aberrant cleavage of TDP-43 enhances aggregation and cellular toxicity.
769 *Proc Natl Acad Sci U S A* **106**, 7607-7612 (2009).
770 https://doi.org/10.1073/pnas.0900688106
771 46 Li, H. R. *et al.* The physical forces mediating self-association and phase-separation in the
772 C-terminal domain of TDP-43. *Biochim Biophys Acta Proteins Proteom* **1866**, 214-223
773 (2018). https://doi.org/10.1016/j.bbapap.2017.10.001
774 47 Prasad, A., Sivalingam, V., Bharathi, V., Girdhar, A. & Patel, B. K. The amyloidogenicity of
775 a C-terminal region of TDP-43 implicated in Amyotrophic Lateral Sclerosis can be affected
776 by anions, acetylation and homodimerization. *Biochimie* **150**, 76-87 (2018).
777 https://doi.org/10.1016/j.biochi.2018.05.003
778 48 Guo, W. *et al.* An ALS-associated mutation affecting TDP-43 enhances protein
779 aggregation, fibril formation and neurotoxicity. *Nat Struct Mol Biol* **18**, 822-830 (2011).
780 https://doi.org/10.1038/nsmb.2053
781 49 Jiang, L.-L. *et al.* Structural Transformation of the Amyloidogenic Core Region of TDP-43
782 Protein Initiates Its Aggregation and Cytoplasmic Inclusion. *Journal of Biological Chemistry*
783 **288**, 19614-19624 (2013). https://doi.org/10.1074/jbc.m113.463828
784 50 Pakravan, D. *et al.* Liquid-Liquid Phase Separation Enhances TDP-43 LCD Aggregation but
785 Delays Seeded Aggregation. *Biomolecules* **11** (2021).
786 https://doi.org/10.3390/biom11040548
787 51 Rollin, R., Joanny, J. F. & Sens, P. Physical basis of the cell size scaling laws. *Elife* **12** (2023).
788 https://doi.org/10.7554/eLife.82490
789 52 Mao, T. *et al.* Stabilizing effect of amino acids on protein and colloidal dispersions. *Nature*
790 **645**, 915-921 (2025). https://doi.org/10.1038/s41586-025-09506-w
791 53 Sun, Y. *et al.* Physiologically Important Electrolytes as Regulators of TDP-43 Aggregation
792 and Droplet-Phase Behavior. *Biochemistry* **58**, 590-607 (2019).
793 https://doi.org/10.1021/acs.biochem.8b00842
794 54 Capitini, C. *et al.* Full-length TDP-43 and its C-terminal domain form filaments in vitro
795 having non-amyloid properties. *Amyloid* **28**, 56-65 (2021).
796 https://doi.org/10.1080/13506129.2020.1826425

55 Lin, P. H. *et al.* TDP-43 Amyloid Fibril Formation via Phase Separation-Related and -Unrelated Pathways. *ACS Chem Neurosci* **15**, 3767-3775 (2024). https://doi.org/10.1021/acschemneuro.4c00503

56 Esposto, J. C. & Martic, S. Phosphorylated TAR DNA-binding protein-43: Aggregation and antibody-based inhibition. *Biochim Biophys Acta Mol Basis Dis* **1867**, 166234 (2021). https://doi.org/10.1016/j.bbadis.2021.166234

57 Shaner, N. C. *et al.* A bright monomeric green fluorescent protein derived from Branchiostoma lanceolatum. *Nature Methods* **10**, 407-409 (2013).

58 Gadella, T. W. J., Jr. *et al.* mScarlet3: a brilliant and fast-maturing red fluorescent protein. *Nat Methods* **20**, 541-545 (2023). https://doi.org/10.1038/s41592-023-01809-y

59 Goedhart, J. *et al.* Structure-guided evolution of cyan fluorescent proteins towards a quantum yield of 93%. *Nat Commun* **3**, 751 (2012). https://doi.org/10.1038/ncomms1738

60 Schmidt, H. B., Barreau, A. & Rohatgi, R. Phase separation-deficient TDP43 remains functional in splicing. *Nat Commun* **10**, 4890 (2019). https://doi.org/10.1038/s41467-019-12740-2

61 Nakagawa, C., Nishimura, S., Senda-Murata, K. & Sugimoto, K. A rapid and simple method of evaluating the dimeric tendency of fluorescent proteins in living cells using a truncated protein of importin alpha as fusion tag. *Biosci Biotechnol Biochem* **76**, 388-390 (2012). https://doi.org/10.1271/bbb.110677

62 Mohanty, P. *et al.* A synergy between site-specific and transient interactions drives the phase separation of a disordered, low-complexity domain. *Proc Natl Acad Sci U S A* **120**, e2305625120 (2023). https://doi.org/10.1073/pnas.2305625120

63 Dubinski, A. *et al.* Stress granule assemblyin vivois deficient in the CNS of mutant TDP-43 ALS mice. *Human Molecular Genetics* **32**, 319-332 (2023). https://doi.org/10.1093/hmg/ddac206

64 Yan, X. *et al.* Intra-condensate demixing of TDP-43 inside stress granules generates pathological aggregates. *Cell* **188**, 4123-4140 e4118 (2025). https://doi.org/10.1016/j.cell.2025.04.039

65 Wang, J. & Bell, L. R. The Sex-lethal amino terminus mediates cooperative interactions in RNA binding and is essential for splicing regulation. *Genes Dev* **8**, 2072-2085 (1994). https://doi.org/10.1101/gad.8.17.2072

66 Wang, J., Dong, Z. & Bell, L. R. Sex-lethal interactions with protein and RNA. Roles of glycine-rich and RNA binding domains. *J Biol Chem* **272**, 22227-22235 (1997). https://doi.org/10.1074/jbc.272.35.22227

67 Ryan, V. H. *et al.* Mechanistic View of hnRNPA2 Low-Complexity Domain Structure, Interactions, and Phase Separation Altered by Mutation and Arginine Methylation. *Mol Cell* **69**, 465-479 e467 (2018). https://doi.org/10.1016/j.molcel.2017.12.022

68 Freibaum, B. D., Chitta, R. K., High, A. A. & Taylor, J. P. Global analysis of TDP-43 interacting proteins reveals strong association with RNA splicing and translation machinery. *J Proteome Res* **9**, 1104-1120 (2010). https://doi.org/10.1021/pr901076y

69 Sear, R. P. Dishevelled: a protein that functions in living cells by phase separating. *Soft Matter* **3**, 680-684 (2007). https://doi.org/10.1039/b618126k

70 Kang, K., Shi, Q., Wang, X. & Chen, Y.-G. Dishevelled phase separation promotes Wnt signalosome assembly and destruction complex disassembly. *Journal of Cell Biology* **221** (2022). https://doi.org/10.1083/jcb.202205069

71 Wang, F. & Zhang, Y. Physiology and pharmacological targeting of phase separation. *J Biomed Sci* **31**, 11 (2024). https://doi.org/10.1186/s12929-024-00993-z

Figure

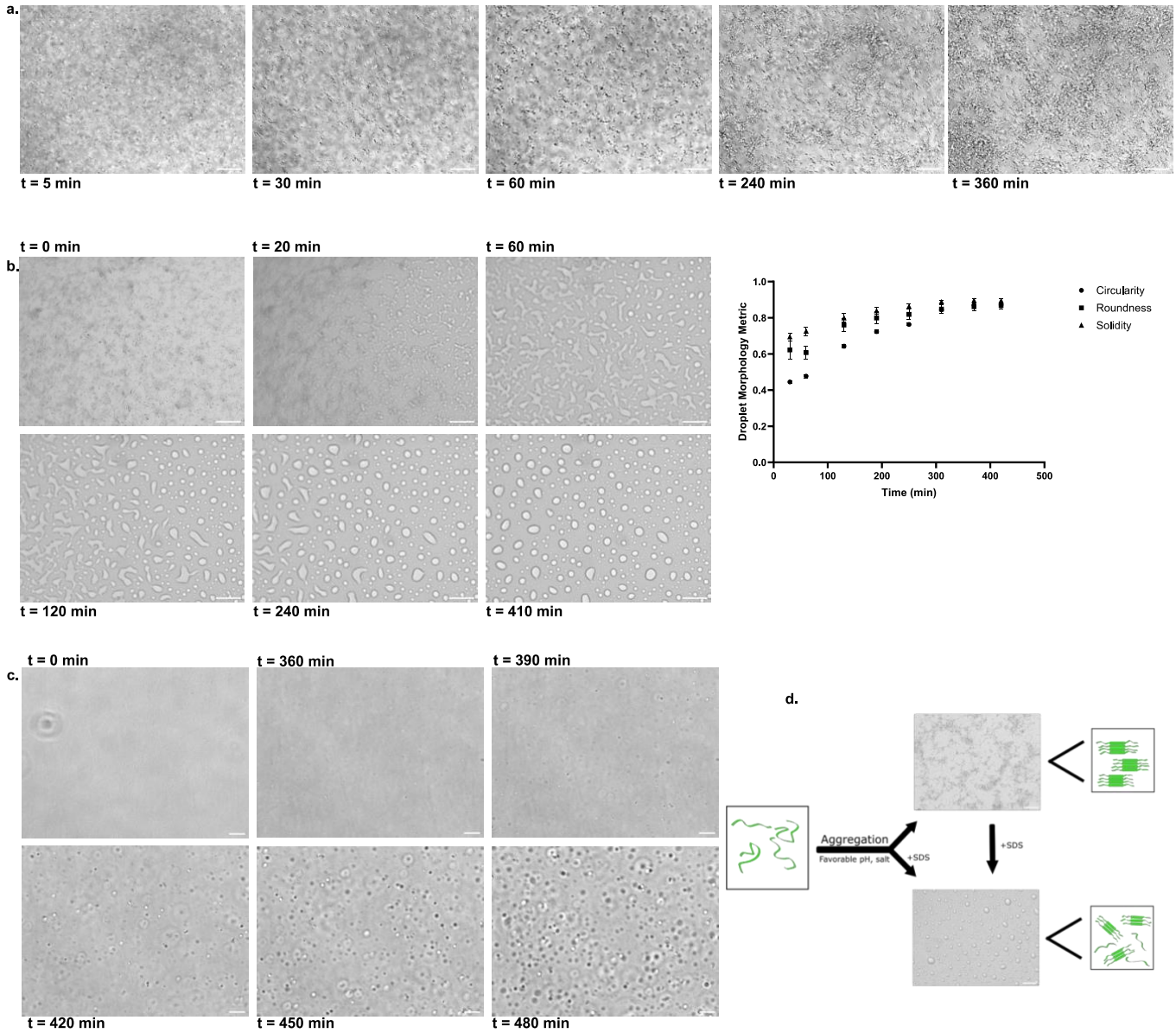

Figure 1. Three-phase transition of recombinant full-length TDP-43 induced by charge modulation

a Gradual formation of solid aggregates from soluble TDP-43 at pH 6 and 0.5 M NaCl. Scale bar is 40μm. **b** Solid aggregates converted into a hydrogel upon addition of SDS (final concentration 0.03%), then progressively transformed into spherical droplets over 7 hours. Time notations begin after addition of SDS. Scale bar is 40μm. **c** The diagram on the right illustrates the time-dependent

872 morphological changes measured by circularity, roundness, and solidity (see Materials and
873 Methods). Error bar is Standard Error of the Mean. **d** Droplets formed directly from solution
874 following SDS addition, with the most pronounced transition occurring between the 6th and 8th
875 hour. Scale bar is 20μm. **e** Schematic representation showing how TDP-43 can transition among
876 all three phases through controlled induction.
877

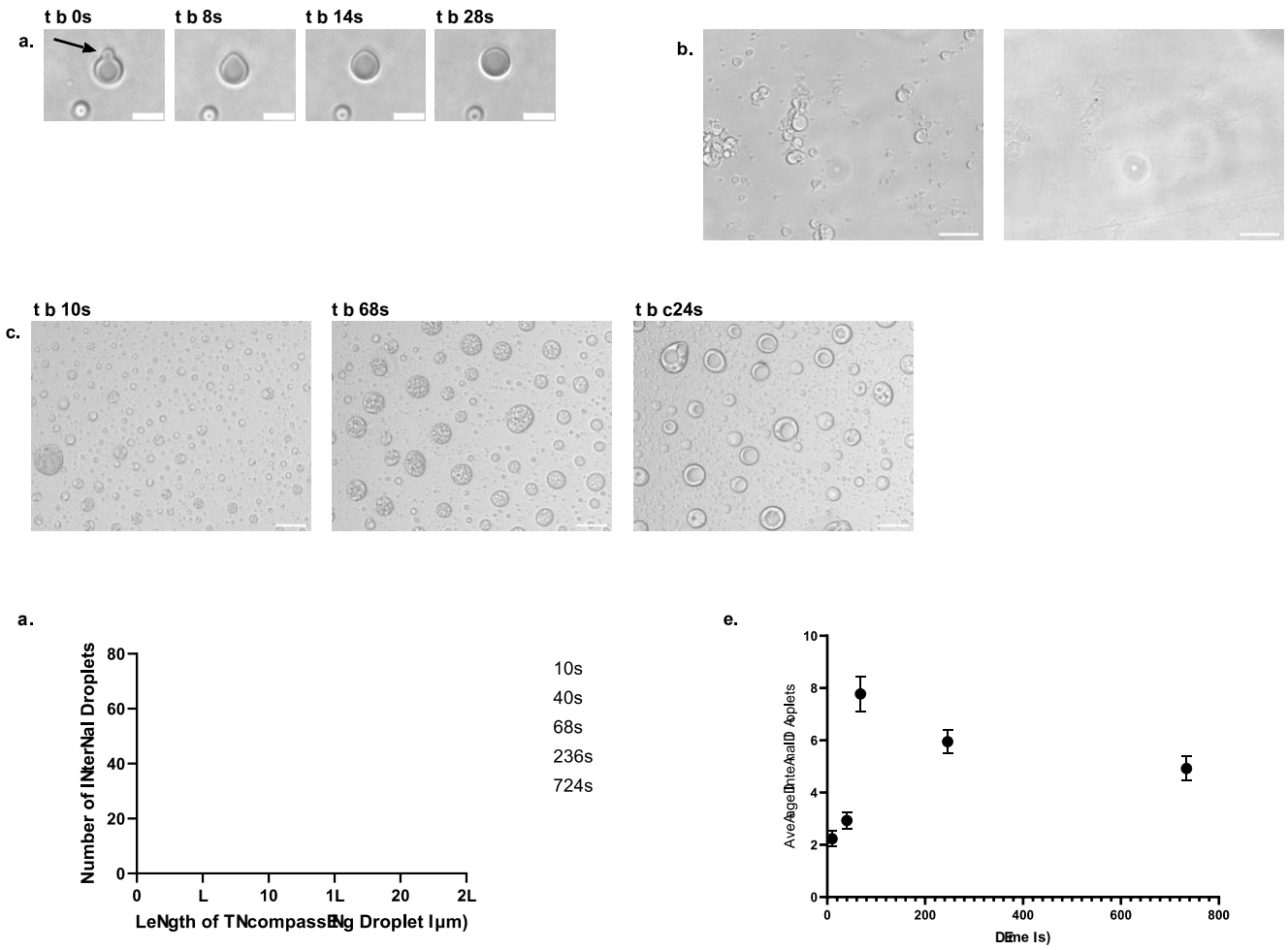

Figure 2. Droplets induced from solid aggregates exhibit liquid-like properties

a Time-lapse images showing a small droplet (arrow) gradually merging with a larger droplet. Scale bar is 10µm. **b** Droplets derived from aggregates dissolve upon treatment with 1,6-hexanediol, consistent with typical LLPS behavior. Scale bar is 40µm. **c** Formation of multi-emulsion droplets upon addition of glycine (50 mM) to initial aggregate-derived droplets. Time indications begin after addition of glycine. Scale bar is 20µm. The transition occurs over on the scale of minutes, progressing from small droplets (top left) to multiple inner droplets encapsulated within larger outer droplets (top middle), and finally to fused, larger droplets (top right). Bottom left: **d** Graph showing the number of internal droplets (left Y-axis) versus the size of the encompassing droplet (X-axis) and time in seconds (right Y-axis). **e** Bottom right: Graph

904 displaying changes in average number of internal droplets per encompassing droplet over time.

905 Error bars are Standard Error of the Mean.

906

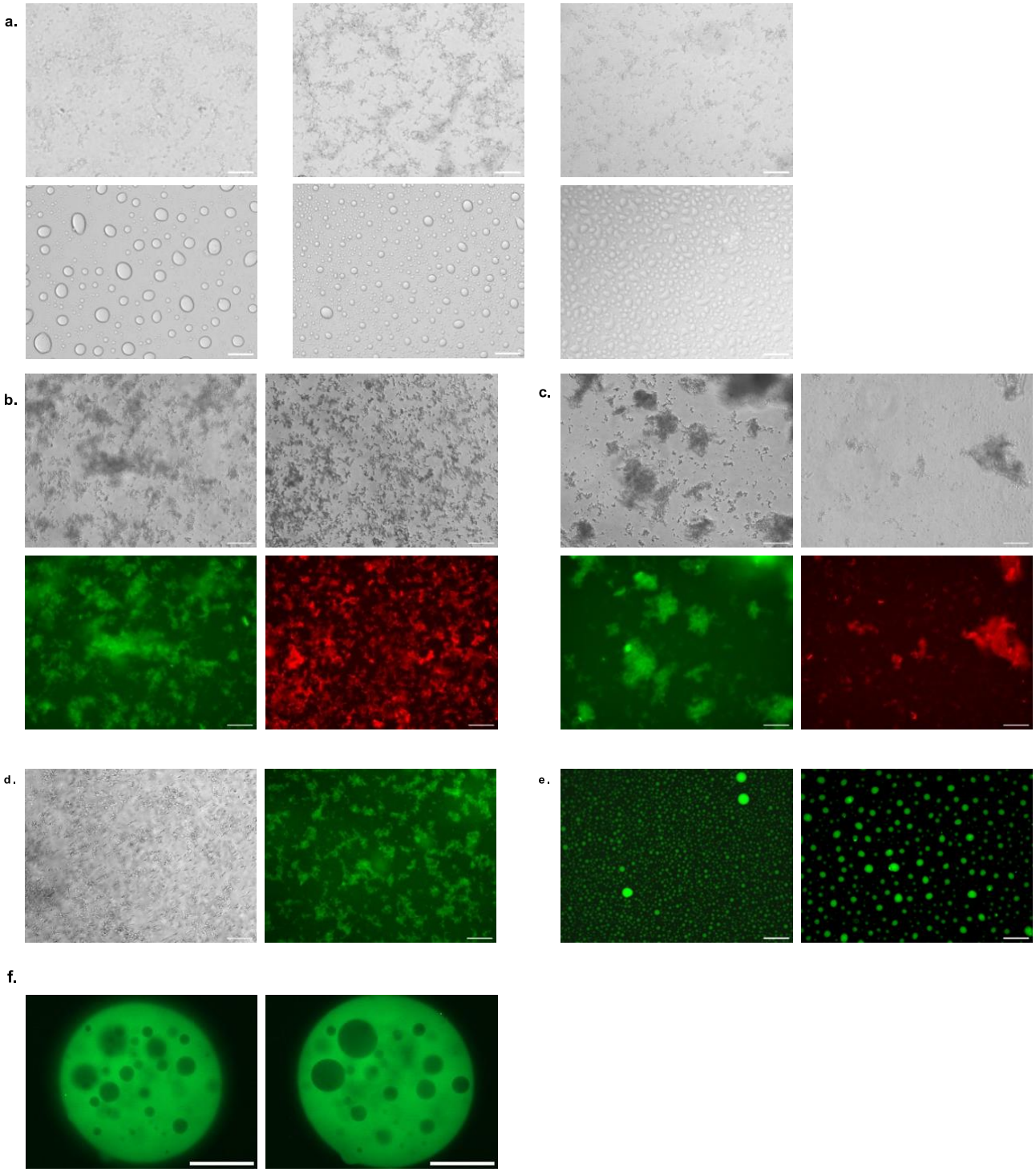

Figure 3. TDP-43, TDP-CTD, and hnRNPH1 form amyloid-positive aggregates and droplets

a Side-by-side comparison of solid aggregates formed by inducing soluble TDP-43, TDP-CTD, and hnRNPH1 at pH 6.0 and 0.5 M NaCl (top), and droplets formed after further addition of SDS

933 (final concentration 0.03%) (bottom). Scale bar is 20μm. **b-d** Aggregates formed by TDP-43 (**b**)
934 and TDP-CTD (**c**) stain positive with ThT and Congo Red (top: bright field; bottom: fluorescence
935 images). **d** hnRNPH1 also stains positive for ThT. Scale bar is 40μm. **e** Representative data
936 showing droplets formed by TDP-43 and TDP-CTD exhibiting ThT staining. Scale bar is 40μm. **f**
937 Multi-emulsion droplet formed upon addition of glycine (50 mM) with ThT included; shown are
938 fluorescence images from a representative Z-stack acquired using Cytation10 (40×). The z-
939 distance between the two slices is 20μm. Scale bar is 100μm.
940
941

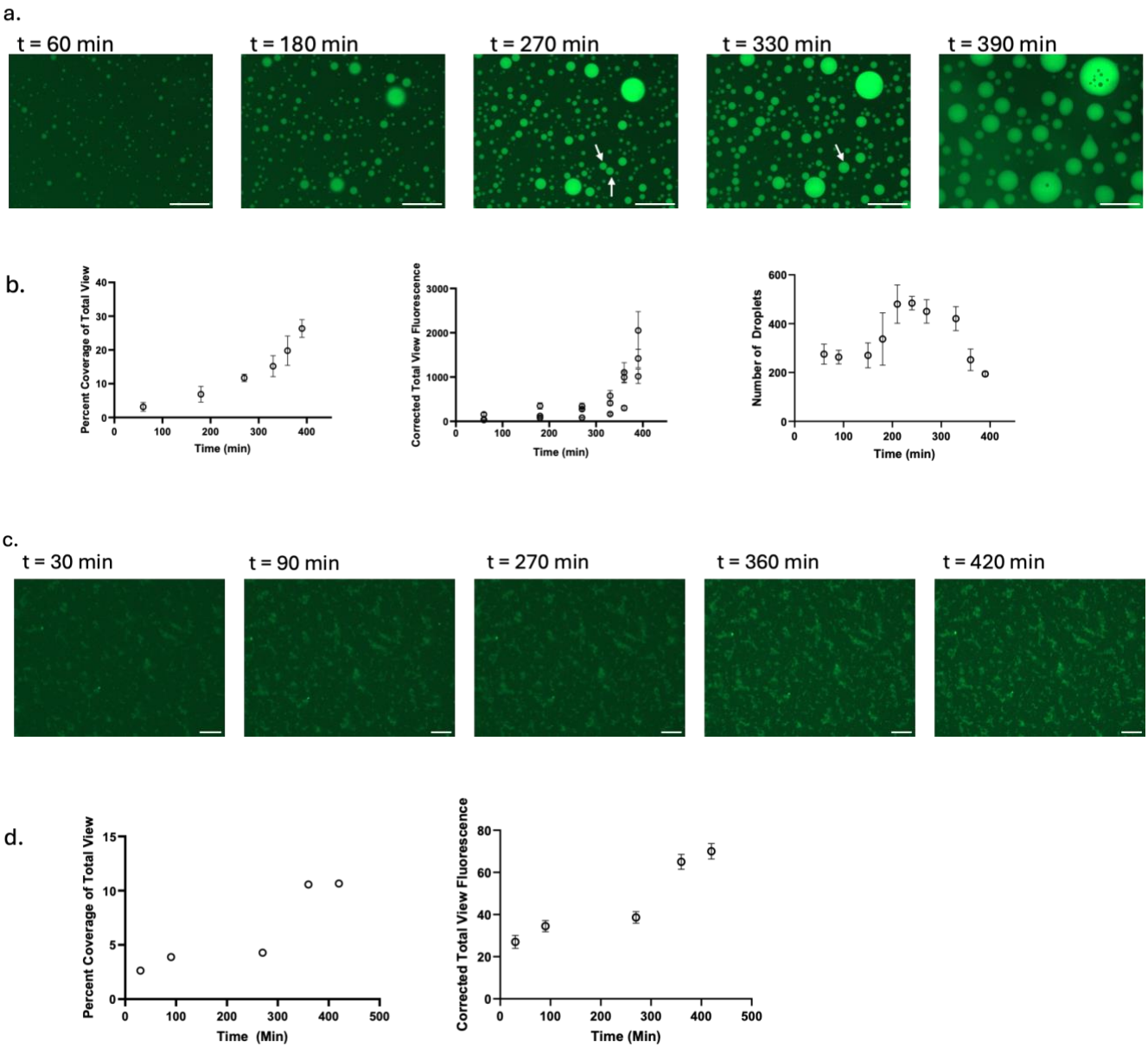

Figure 4. Time course of amyloid-containing droplet and solid aggregate formation

a Still photos taken at indicated time points from a time-lapse series of fluorescence image capturing of droplets formation from soluble solution of TDP-43. ThT was added to protein solution before addition of SDS (0.03% final concentration) at time 0. Arrows point to example droplets in merging process. Scale bar is 100μm. **b** Quantitative analysis of count, percentage of view covered, and Corrected Total View Fluorescence (CTVF) of the droplets formed from 3 separate, non-overlapping views of the same time lapse course. Droplet count and area covered are

953 averaged from the 3 views while CTVF is presented from each time point and view. **c** Still photos
954 taken at indicated time points from a time-lapse series of fluorescence image capturing solid
955 aggregates from soluble solution of TDP-43. ThT was added to protein solution before addition of
956 1M Tris-HCl pH6 and 5M NaCl at 10% final volume at time 0. Scale bars are 50μm. All reactions
957 were carried out at room temperature, ~25°C. **d** Quantitative analysis of view covered and
958 fluorescence intensity of the solid aggregates formed. Data came from 1 representative view of
959 the time lapse.
960

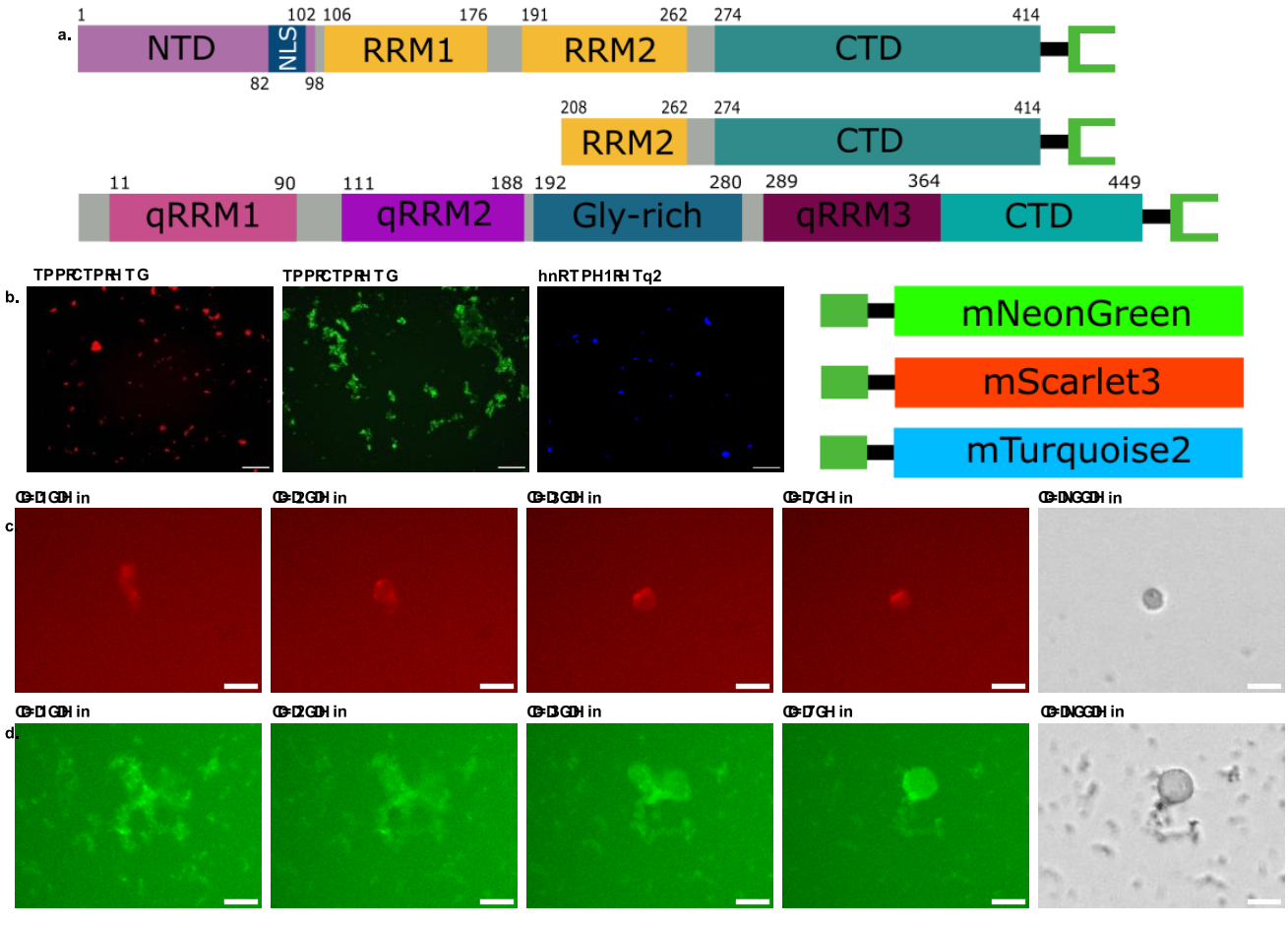

Figure 5. Labeling phase-transition proteins with switchable fluorescent tags

a Schematic representation of protein domains fused with SpyTag/SpyCatcher modules. **b** Solid aggregates formed by TDP-43–mNeonGreen (left), TDP-CTD–mScarlet3 (middle), and hnRNPH1–mTurquoise2 (right) under induction conditions. Scale bar is 40µm. **c** Time-lapse images showing TDP-43–mNeonGreen and (**d**) TDP-CTD–mScarlet3 transitioning from solid aggregates into droplets; the corresponding bright-field image for the final fluorescence frame is shown on the right. Time notations begin after addition of SDS. Scale bars are 10µm.

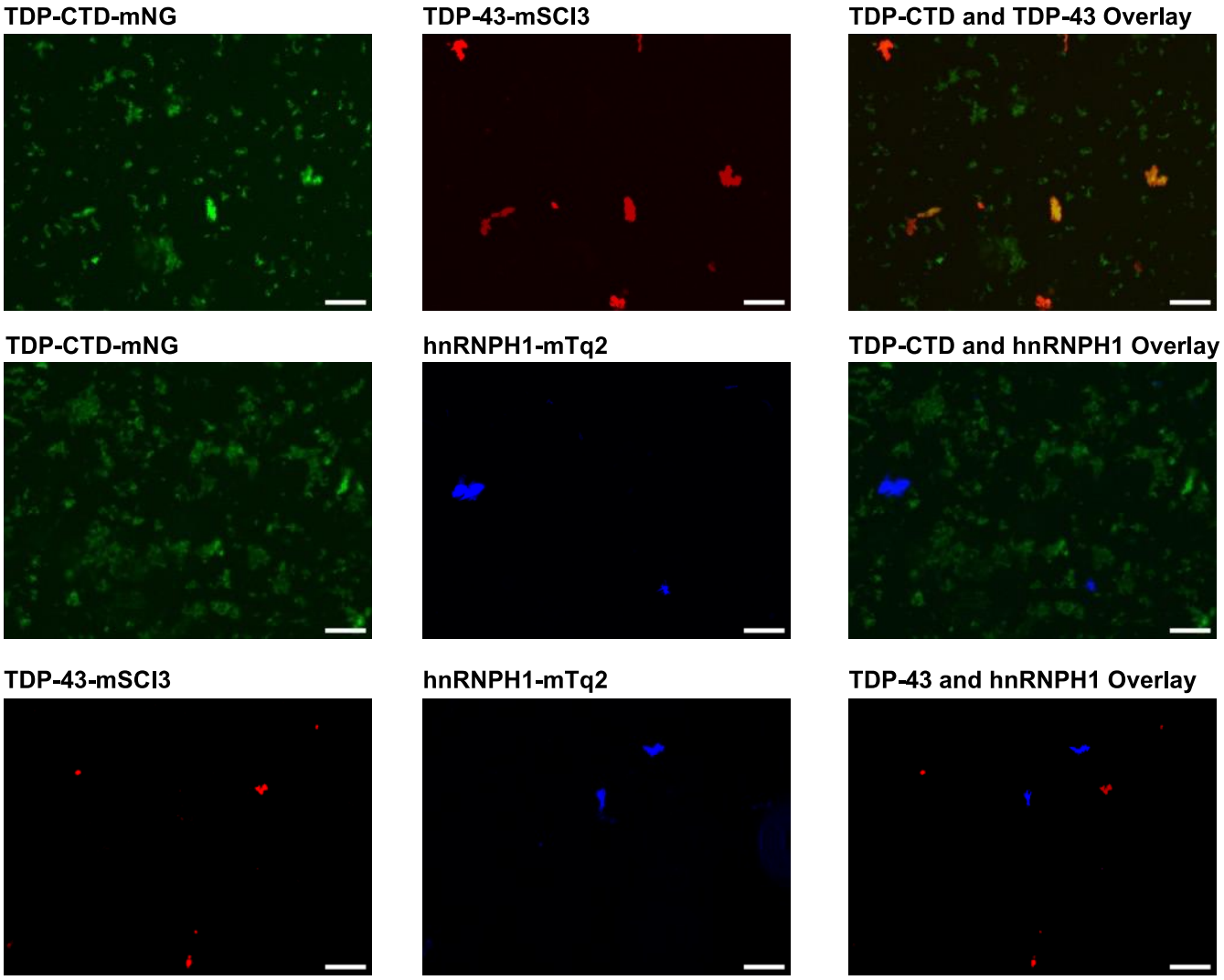

Figure 6. Seeding of phase transition depends on protein compatibility

Pairwise mixing of TDP-CTD–mNeonGreen (mNG), TDP-43–mScarlet3 (mSCI3), and hnRNPH1–mTurquoise2 (mTq2) in solution prior to induction to form aggregates. Coaggregates between TDP-CTD–mNeonGreen and TDP-43–mScarlet3 appear as yellow-orange due to fluorescence overlap. Scale bar is 20μm.